Andrew P. Baumann[1]
U.S. Food and Drug Administration,
Center for Devices and Radiological Health,
Office of Science and Engineering Laboratories,
10903 New Hampshire Avenue,
Building 62, Room 2110,
Silver Spring, MD 20993
e-mail: Andrew.Baumann@fda.hhs.gov

Oleg Vesnovsky
U.S. Food and Drug Administration,
Center for Devices and Radiological Health,
Office of Science and Engineering Laboratories,
10903 New Hampshire Avenue,
Building 62, Room 2227,
Silver Spring, MD 20993
e-mail: Oleg.Vesnovsky@fda.hhs.gov

L. D. Timmie Topoleski
Department of Mechanical Engineering,
University of Maryland, Baltimore County,
1000 Hilltop Circle,
Baltimore, MD 21250
e-mail: topolesk@umbc.edu

Finn E. Donaldson
U.S. Food and Drug Administration,
Center for Devices and Radiological Health,
Office of Product Evaluation and Quality,
OHT2: Office of Cardiovascular Devices,
10903 New Hampshire Avenue,
Building 66, Room 1253,
Silver Spring, MD 20993
e-mail: Finn.Donaldson@fda.hhs.gov

Nicole L. L. McMinn
U.S. Food and Drug Administration,
Center for Devices and Radiological Health,
Office of Product Evaluation and Quality,
OHT6: Office of Orthopedic Devices,
10903 New Hampshire Avenue,
Building 66, Room 4435,
Silver Spring, MD 20993
e-mail: Nicole.McMinn@fda.hhs.gov

Amelia Vignola
U.S. Food and Drug Administration,
Center for Devices and Radiological Health,
Office of Science and Engineering Laboratories,
10903 New Hampshire Avenue,
Building 62,
Silver Spring, MD 20993
e-mail: Amelia.Vignola@fda.hhs.gov

Matthew Di Prima
U.S. Food and Drug Administration,
Center for Devices and Radiological Health,
Office of Science and Engineering Laboratories,
10903 New Hampshire Avenue,
Building 62, Room 2124,
Silver Spring, MD 20993
e-mail: Matthew.Diprima@fda.hhs.gov

Specimen-Specific Finite Element Models for Predicting Fretting Wear in Total Hip Arthroplasty Tapers

Products from fretting wear and corrosion in the taper junction of total hip arthroplasty (THA) devices can lead to adverse local tissue reactions. Predicting damage as a function of design parameters would aid in the development of more robust devices. The objectives of this study were to develop an automated method for identifying areas of fretting wear on THA taper junctions, and to assess the predictive ability of a finite element model to simulate fretting wear in THA taper junctions. THA constructs were fatigue loaded, thus inducing damage on the stem taper. An automated imaging and analysis algorithm quantified fretting wear on the taper surfaces. Specimen-specific finite element models were used to calculate fretting work done (FWD) at the taper junction. Simulated FWD was correlated to imaged fretting wear. Results showed that the automated imaging approach identified fretting wear on the taper surface. Additionally, finite element models showed the greatest predictive ability for tapers exhibiting distal contact. Finite element models predicted an average of 30.3% of imaged fretting wear. With additional validation, the imaging and finite element techniques may be useful to manufacturers and regulators in the development and review of new THA devices. [DOI: 10.1115/1.4045904]

[1]Corresponding author.
Manuscript received March 8, 2019; final manuscript received December 2, 2019; published online February 24, 2020. Assoc. Editor: Sara Wilson.

Introduction

Over 300,000 people receive a total hip arthroplasty (THA) each year in the United States [1,2]. It is the second most common joint replacement procedure following total knee arthroplasty. Current THA devices consist of multiple components, and generally include a cup and liner on the acetabular (pelvic) side, and a stem, head, and optionally a sleeve on the femoral side. A majority of these components can be obtained in different sizes. This modular design allows the surgeon freedom to configure the implant during surgery to optimally match the patient's anatomy [3–7]. However, modularity can lead to complications like component mismatch, disassociation, fracture, and wear at mating surfaces [3–5,7–10]. One area of concern is the junction between femoral stems and heads. The head and neck are most often joined with a small angle taper [11]. While effective in joining the two components, in vivo fatigue loading associated with normal walking can cause unwanted micromotion between the stem and head, leading to fretting wear and corrosion [5,7,8,10,12–15]. This damage can gradually release metal ions and particles, causing adverse local tissue reactions and osteolysis that may ultimately cause device failure and the need for revision surgery [7,15–18]. Understanding the design features that influence such failures may lead to improved devices and reduced adverse outcomes.

Stem-head taper junction parameters—including device material, loading rate, construct stiffness, angular mismatch, contact length, surface finish, and other features—have all been shown to influence micromotion, fretting wear, and corrosion [12,19–22]. In addition, because the components are assembled in vivo, the assembly force and impact technique also affect the performance of the modular connection, its likelihood of loosening, and the potential for adverse events [23–27]. The prevalence of fretting wear has led to the development of standardized scoring systems and advanced imaging techniques that allow for consistent evaluation (grading) of fretting wear and corrosion of taper junctions [12,28–30]. However, despite being well characterized, taper damage remains difficult to predict. A method is needed for determining the likelihood of fretting wear in a stem-head taper junction so that devices can be designed to reduce the rate of in vivo failure.

Numerical techniques such as finite element analysis (FEA) may provide a method for predicting in vivo taper junction performance. FEA provides a computational framework where design parameters can be isolated and their relative contribution to mechanical integrity can be quantified. For example, FEA has been used to investigate the effect of manufacturing tolerance on micromotion of tapered junctions [31]. Wear, micromotion, contact stress, and disassembly force at the head–neck interface have also been quantified with finite element modeling [32,33]. Recently, a computational model was developed to investigate the relative influence of taper design parameters and load on fretting work done (FWD) as a predictor for taper wear and corrosion performance [34]. Experimental constructs were used to validate the micromotion predicted by the model, but the predicted FWD was not correlated to physical fretting wear and corrosion. Validating the FWD predictions of this model may allow for more accurate predictions of fretting wear in vivo.

The goal of this study was to develop a finite element model to predict fretting in THA constructs. Using previously described techniques, the modular surfaces of fatigue tested taper constructs were fully imaged [29]. To avoid observer bias, an automated technique was developed to identify areas of fretting wear on experimental taper connections. The FWD finite element framework was used to create specimen-specific models of experimental taper connections. The ability of the automated quantification method and finite element model to identify and predict fretting wear in THA tapers was evaluated.

Methods

Bench Testing. Each experimental taper connection consisted of a femoral stem with a male taper and a femoral head with a corresponding female taper. Taper connections ($n = 10$) were

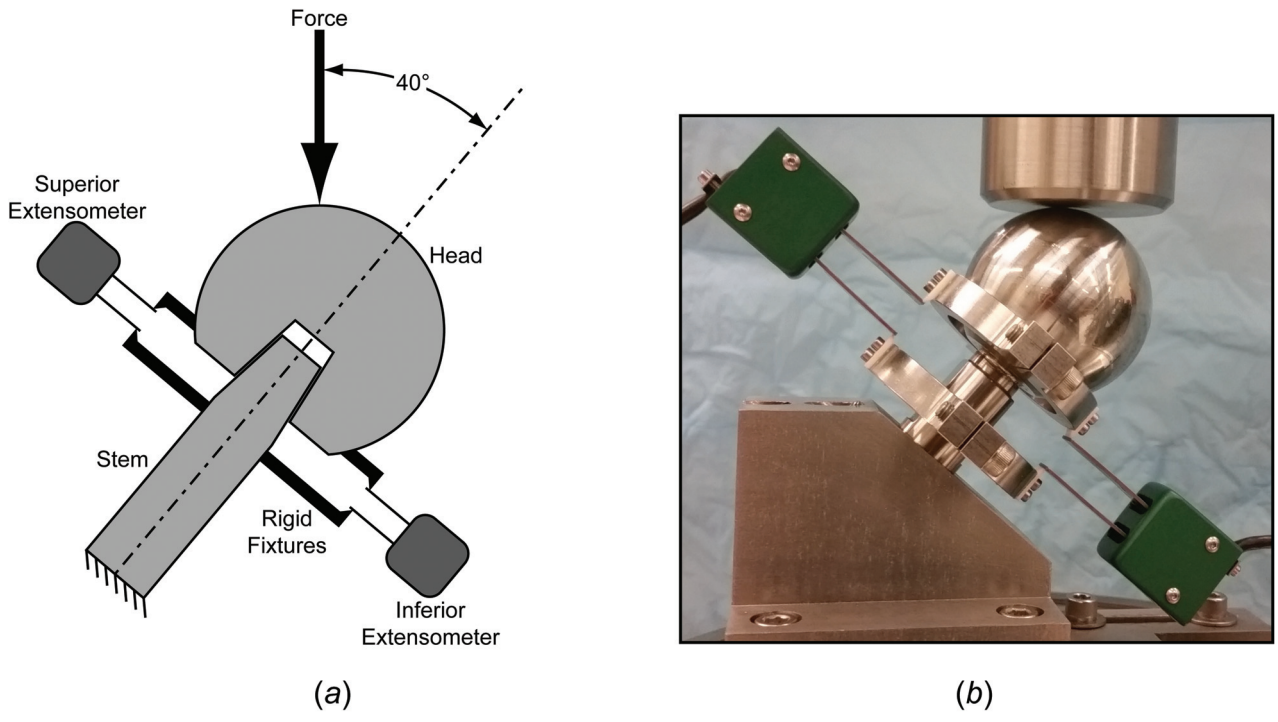

Fig. 1 (*a*) **Experimental setup of the THA constructs during fatigue loading. The femoral head is first impacted on the femoral stem. The femoral stem is attached to a base that orients the construct 40 deg from vertical and the direction of applied load. Extensometers placed on the superior and inferior sides of the construct measure relative motion between stem and head via rigid fixtures. (*b*) Photograph of the experimental setup.**

manufactured from a single lot of CoCr alloy (ASTM F1537, M. Vincent & Associates, Minneapolis, MN), ensuring consistent material properties throughout the specimens. Stem and head taper angles were measured with a Talyrond 585 out-of-roundness machine (Taylor Hobson, Leicester, UK). Heads were fixed onto the stems using an impact load of 5000 N produced by a custom-built drop hammer. Impact loads were previously measured while a surgeon reproduced the clinical procedure for ball placement on a trunnion that was attached to a load cell. Assemblies were attached to a uni-axial load frame (MTS, model 312.21, Minneapolis, MN) using a custom designed load fixture such that the axis of the stem was oriented 40 deg off the vertical axis and line of applied load (Fig. 1). A sinusoidal cyclic load (min = 280, max = 2800 N) was applied to the femoral heads at a rate of 10 Hz for 10×10^6 cycles. The 2800 N load was chosen as the average of the ISO 7206-4 (2300 N) and ASTM F1875 (3300 N) loads [35,36]. The loading frequency was within the range prescribed by ISO 7206-4 (1–30 Hz). All tests were conducted in phosphate buffered saline at 37 °C. Relative motions of the stems and heads were measured during fatigue loading using extensometers (Epsilon Technology, Corp., Jackson, WY) placed on the superior and inferior sides of the constructs.

Constructs were disassembled and the taper surfaces of the stems were imaged using the digital mosaic method (DMM), described in detail elsewhere [29]. Briefly, the taper surfaces were sequentially imaged at high magnification along the circumferential and longitudinal directions (HIROX KH-7700, HIROX-USA, Hackensack, NJ) (Fig. 2(*a*)). The high magnification images were digitally stitched together using the open source imaging editor GIMP (GNU Image Manipulation Program) to create Cartesian representations of the stem taper surfaces (Fig. 2(*b*)). Unaffected areas of the taper surface (areas of minimal nonvisible wear) exhibited longitudinal light-to-dark banding caused by the variation in reflected light when imaging the curved surface of the taper. Individual photographs are darker in the center and brighten toward the edges (i.e., a circumferential brightness gradient), resulting in axially oriented light-to-dark bands, with one band for each photograph in the circumferential direction. In unaffected areas of the taper, 40 distinct light-dark bands are visible, corresponding to the 40 pictures taken around the circumference of the taper. In damaged areas, fretting wear and corrosion disrupt surface reflection and inhibit banding.

A discrete Fourier transform (DFT) technique was used to identify fretting wear areas in the stitched images. DMM images were converted to grayscale, scaled to decrease image size, and smoothed using a Gaussian filter (sigma = 4.0) (Fig. 3(*a*)). For each pixel, a DFT identified the dominant frequency, f_D, of the grayscale image intensity (from 0 to 255) as a function of position over a span of pixels ranging over ±250 pixels in the circumferential direction (Fig. 3(*b*)). The dominant frequency was then assigned to the corresponding pixel and a frequency map was generated for the entire image (Fig. 3(*c*)). In unaffected areas where wear is so minimal that it is nonvisible, the dominant frequency, f_D, corresponds to the number of pictures (40) per the number of pixels (2200) in the circumference of the image (0.018 = 40 ÷ 2200). In damaged areas, where the regular light-to-dark banding is disrupted, the dominant frequency, f_D, is measurably different than this value. Binary images, indicating damaged or undamaged surface, were created by assigning a damage threshold to the frequency maps and subsequently assigning a greyscale intensity of white to the undamaged and black to the damaged pixels (Fig. 3(*d*)). A parametric study varied the Gaussian filter (smooths

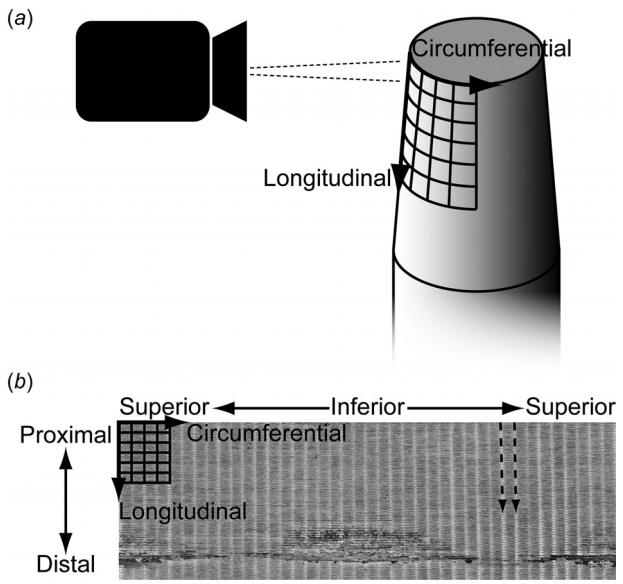

Fig. 2 (*a*) After disassembly, the stem taper is imaged using the DMM. Here, high magnification images are taken around the circumference and length of the taper. (*b*) The images are digitally stitched together to create a Cartesian map of the taper surface. The imaging technique produces light-to-dark bands running in the longitudinal (vertical) direction. Dashed arrows indicate two sequential light bands. There are 40 bands in total, one for each image in the circumferential (horizontal) direction.

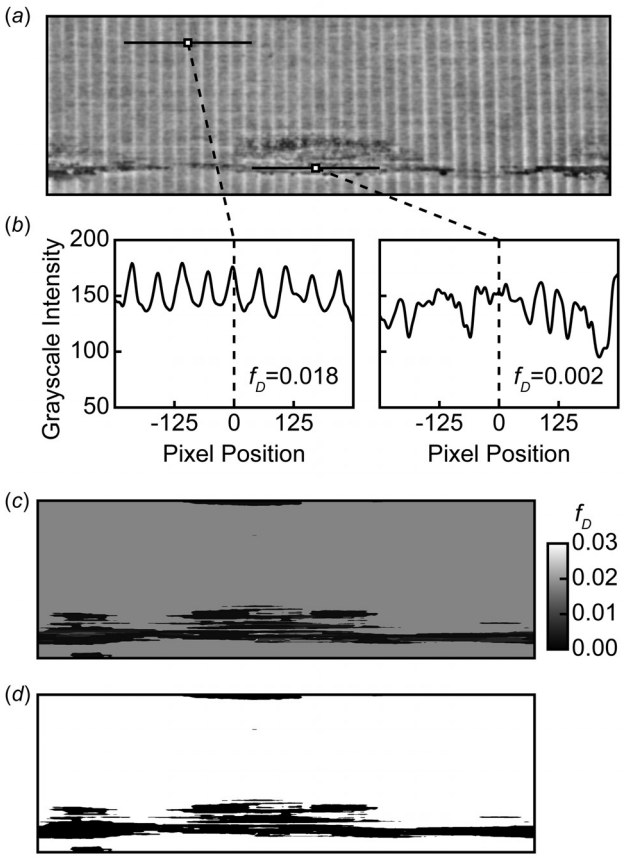

Fig. 3 (*a*) DMM images are converted to grayscale, scaled, and Gaussian filtered. (*b*) For each pixel in the image, the grayscale image intensity (0–255) is measured for a range of ±250 pixels in the circumferential direction. A discrete Fourier transform is used to calculate the dominant frequency, f_D, of the image intensity response. Undamaged areas (left) have a dominant frequency corresponding to the number of images per circumference. Damaged areas (right) have a dominant frequency significantly greater or less than this value. (*c*) A frequency map is generated for the taper surface. (*d*) The map is thresholded to create a binary image identifying the damaged (black) and undamaged areas (white).

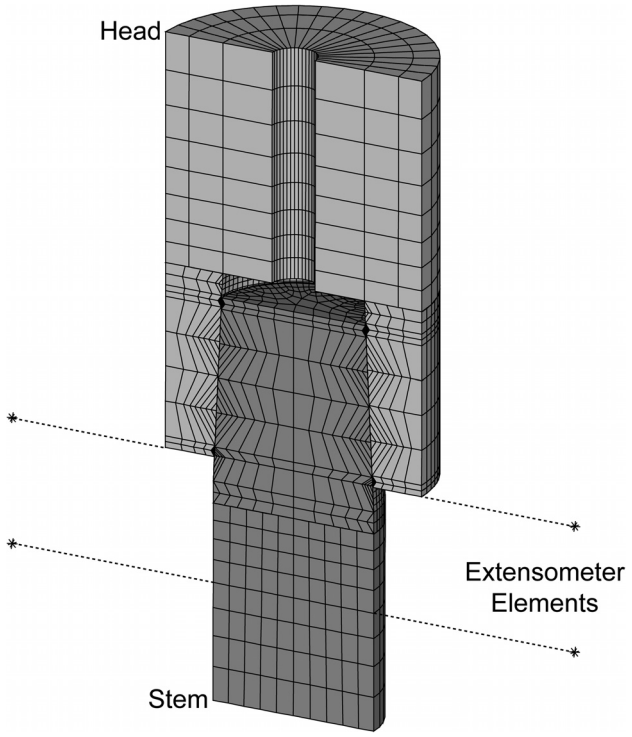

Fig. 4 Section view of the finite element model. Stem geometries are approximated as a cylindrical post with male taper, and head geometries are approximated as a cylindrical sleeve with female taper. Single node elements replicated the extensometers and load fixtures. These were rigidly tied to the stem and head surfaces, and their relative displacements were tracked throughout the load cycle.

image) from 0.5 to 6.0 and pixel span (range of discrete Fourier transform) from ±50 to ±500. Filter and span values of 4.0 and ±250, respectively, most consistently identified damaged and undamaged areas.

Finite Element Analysis. Specimen-specific finite element models ($n = 10$) were created using a previously validated finite element framework [34]. Validation of micromotion was achieved through direct comparison of modeled results to measured experimental micromotions. Analyses were implicit and quasi-static (Mechanical APDL, Release 19.0, ANSYS, Inc., Canonsburg, PA). Stem geometries were approximated as a cylindrical post ending in a male taper, and head geometries were approximated as a cylindrical sleeve encompassing a female taper (Fig. 4). The taper angles measured during bench testing were used to create the specimen-specific model geometries. Volumes near contact areas were meshed with second-order, reduced integration, hexahedral elements to capture high stress gradients associated with contact. Volumes away from contact areas were meshed with first-order hexahedral elements to reduce computational cost. Surface-to-surface contact was specified between stem and head taper surfaces. Contact and target surface elements were placed over the stem and head tapers, respectively. Single-node elements were placed above and below the superior and inferior surfaces, respectively, to replicate the extensometers. The extensometer elements were rigidly tied to the stem and head surfaces so distances between them could be calculated throughout the load cycle in the same way the extensometers measured the distance between the rigid stem and head fixtures. The distal surface of the stem was rigidly constrained in all degrees-of-freedom. Loads acted through a pilot node located at the head center which was rigidly tied to the proximal head surface. Loading was applied in two stages. First, a 5000 N load was applied axially to mimic the impact load and seat the head on the stem. Second, a sinusoidal load was applied 40 deg off axis mimicking the bench test (min = 280, max = 2800 N). The frictional contact between head and stem creates nonlinearity in the model, which may necessitate several load cycles before achieving steady-state. A previous convergence study of ten consecutive load cycles showed convergence of FWD after one load cycle. Therefore, two load cycles were simulated with all results taken from the second cycle. Element size was determined through a previous mesh convergence study where the output variables of contact pressure, micromotion, and FWD converged to 3.0%, 2.3%, and 3.1%, respectively. Element size was evaluated relative to meshes of twice the linear resolution and was locally refined in regions of interest. Details of the convergence studies are provided elsewhere [34]. Output variables at the contact surfaces were contact pressure, P, and micromotion, M. These were used to calculate the fretting work done (FWD = coefficient of friction $\times P \times M$) of one gait cycle over the taper surface. Relative motions between head and stem were also calculated from the distances between extensometer elements.

Material properties assigned to the stem and head were linear-elastic and isotropic, based on the properties of CoCr alloy. A preliminary parametric study investigating coefficient of friction and elastic modulus determined that device modulus had the most influence on micromotion between the head and stem. Elastic modulus was determined through a calibration where it was varied through a range of reported values [37–39]. Modulus was incremented between 200 and 230 GPa until error was minimized between modeled and measured extensometer distances. Calibrated elastic properties were $E = 210$ GPa and $\nu = 0.3$. Contact between the stem and head was implemented with a linear, isotropic, friction law. The coefficient of friction of CoCr on CoCr was assigned to be 0.30 [40].

Fretting work done from the calibrated models ($E = 210$ GPa and $\nu = 0.3$) was plotted on a Cartesian domain and initially had a resolution corresponding to the finite element mesh (32 by 80 elements) (Fig. 5(*a*)). FWD maps were then discretized to have the same pixel resolution as the bench test results (DFT damage maps, ~600 by 2200 pixels) (Fig. 5(*b*)). Binary images of modeled fretting wear were produced by thresholding the FWD maps. The threshold value was based on the average percent of damaged area in DFT maps, 7.7% (Table 1). A critical level of FWD (J/m^2) was determined for each finite element model at the upper 7.7% value of the FWD distribution. All areas having FWD greater than this value were considered damaged. All areas having FWD less than this value were considered undamaged (Fig. 5(*c*)). FWD maps were registered to DFT maps by aligning the circumferential (horizontal) orientation and then trimming the longitudinal (vertical) dimensions to match. The binary FWD maps were compared on a pixel-to-pixel basis to the bench test DFT damage maps. Predictive ability of the simulations was quantified as the amount of DFT damage that was in the same pixel location as modeled FWD damage. This agreement was quantified as both a percentage and areal measure.

A paired Student's t-test was used to test for differences between measured and simulated displacements on the superior and inferior surfaces with significance set at $p \leq 0.05$.

Results

The measured taper angles of the stems and heads along with measured and predicted fretting wear are presented in Table 1. Analysis of construct angular mismatch yielded eight of the ten constructs with neutral to distal (positive) contact: specimens 1, 2, 3, 6, 7, 8, 9, and 10. The remaining two constructs had proximal (negative) contact: specimens 4 and 5. Stem tapers had an average imaged area of 570.7 mm^2, as determined from DMM. The DFT technique identified an average of 44.2 mm^2 of damaged surface, or 7.7% of the total taper surface. This value was used to threshold fretting corrosion of the simulated FWD maps at the upper 7.7%

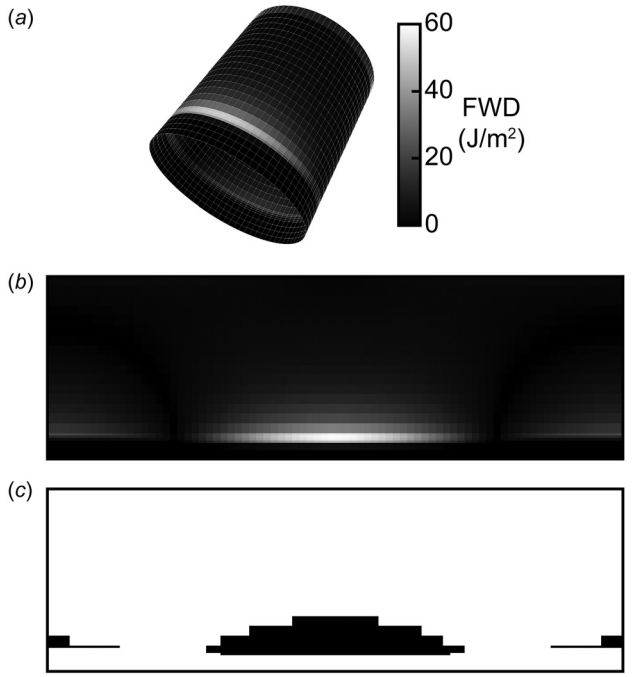

Fig. 5 (*a*) Accumulated FWD over one load cycle was calculated using the pressure, *P*, and micromotion, *M*, data from the FEA. (*b*) The FWD maps are rediscretized to have the same dimensions and resolutions as the DFT damage maps. (*c*) These Cartesian FWD maps are thresholded to create a binary image for predicting the damaged (black) and undamaged areas (white).

of each FWD distribution (Fig. 5(*c*)). The mean (±SD) FWD threshold value across all models was 32.98 (±24.38) J/m^2.

Mean maximum extensometer displacements were 35.46 μm (extension) and 37.60 μm (contraction) on the superior and inferior sides of the construct, respectively (Fig. 6). Calibrating the average simulated extensometer distances to measured average distances produced a modulus for the stem and head of 210 GPa, which was within the range of literature values [37–39]. Mean simulated displacements were 34.04 μm and 38.24 μm for the superior and inferior surfaces, respectively. Differences between measured and simulated displacements on the superior surface ($p = 0.086$) and inferior surface ($p = 0.591$) were not statistically significant.

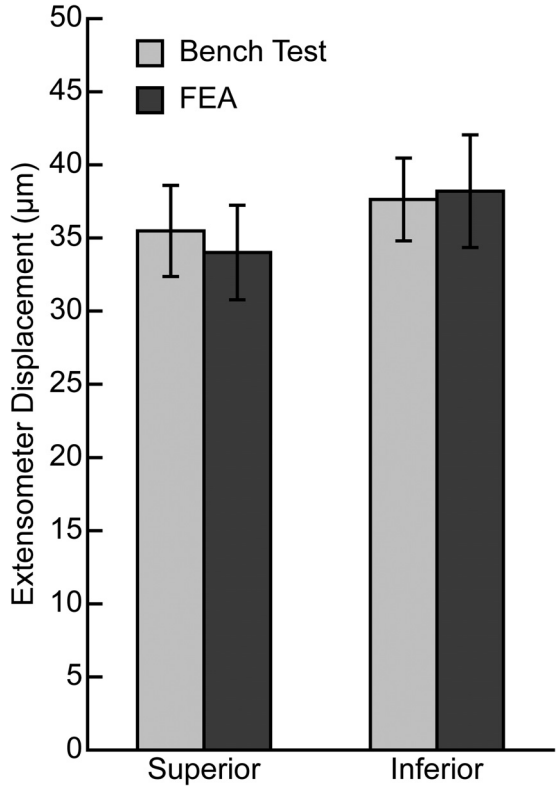

Fig. 6 Relative maximum extensometer displacements between stems and heads over a loading cycle (means and standard deviations). Bench tests measured displacements between rigid fixtures using extensometers. Finite element models calculated displacements between single-node elements that replicated the fixtures and extensometers. Displacements on the superior side are in extension (tension), and displacements on the inferior side are in contraction (compression). Differences between measured and simulated displacements on the superior surface ($p = 0.086$) and inferior surface ($p = 0.591$) were not statistically significant.

An example of the individual DFT and FWD binary damage maps, and a combined map showing their regions of overlap, is given in Fig. 7. Both DFT and FWD damage distributions were dependent upon contact location. Constructs having neutral to distal contact exhibited a DFT map with damage wrapping around

Table 1 Stem angle and head angle denote the measured taper angles of the stems and heads, respectively. Angular mismatch is the difference between the stem and head angles, with positive and negative angular mismatches denoting distal and proximal contact within the taper junctions, respectively. Total image area is the total stem taper surface area as measured by the DMM. DFT area is the area of fretting wear and corrosion on the stem taper surface identified with the DFT technique (magnitude and percentage of total image area). FWD area is the area of fretting wear predicted by the finite element model (magnitude and percentage of DFT area). DFT+FWD area is the common area overlayed by both DFT and FWD.

Specimen	Stem angle (deg)	Head angle (deg)	Angular mismatch (deg)	Total image area (mm^2)	DFT area (mm^2)	DFT area (% of total)	FWD area (mm^2)	FWD area (% of DFT)	DFT + FWD area (mm^2)
1	5.5130	5.5110	0.0020	549.0	33.1	6.0	41.7	64.3	21.3
2	5.5220	5.5125	0.0095	548.7	47.1	8.6	42.0	35.7	16.8
3	5.5300	5.5135	0.0165	613.9	74.5	12.1	46.7	43.3	32.3
4	5.4085	5.5215	−0.1130	448.5	37.2	8.3	34.1	0.0	0.0
5	5.4025	5.5175	−0.1150	572.8	56.8	9.9	43.7	2.6	1.5
6	5.6595	5.5085	0.1510	570.0	29.0	5.1	43.4	49.1	14.2
7	5.6425	5.5065	0.1360	552.6	28.3	5.1	42.3	34.3	9.7
8	5.6645	5.5095	0.1550	568.2	9.2	1.6	43.5	18.1	1.7
9	5.5180	5.5140	0.0040	676.5	63.8	9.4	51.5	29.4	18.7
10	5.5135	5.5140	−0.0005	606.3	62.9	10.4	46.1	26.3	16.5
Mean	5.5374	5.5129	0.0246	570.7	44.2	7.7	43.5	30.3	13.3
Std. dev.	0.0887	0.0042	0.0926	55.3	19.2	3.0	4.2	18.9	9.7

the circumference of the distal end with a concentration on the inferior surface (Fig. 8). Proximally contacting specimens had DFT damage concentrated in the center (longitudinally), and center to superior surface (circumferentially). FWD damage distribution was also dependent upon contact location. FWD distributions were concentrated on the inferior surface of the constructs with the longitudinal position of the FWD concentration corresponding to the contact location: distal concentration for neutral to distal contact and proximal concentration for proximal contact.

The FWD maps generally predicted damage in the correct locations, with the FWD areas being spatially near the DFT damage areas. Overlaying DFT and FWD area ranged from 0.0 to 32.3 mm^2. The percentage of DFT area overlaying FWD area ranged from 0.0 to 64.3%. On average, FWD area coincided with 30.3% of the DFT damage area (Table 1, Fig. 8). Predictive ability was much higher for distally contacting constructs than for proximally contacting. Neutral to distal contacting models predicted an average of 37.6% of the DFT damage. In contrast, specimens four and five exhibited proximal contact, and their models predicted 0.0 and 2.6% of the DFT damage, respectively. In the proximally contacting specimens, FWD maps overestimated the proximal shift of the damage region and underestimated its shift to the superior surface (Fig. 2(*b*) illustrates proximal-distal and superior–inferior orientation on the image maps).

Discussion

Experimental THA constructs were manufactured to quantify fretting wear in the stem-head taper junction. An automated imaging analysis technique was developed using discrete Fourier transforms to identify damaged areas on the taper surfaces. Specimen specific finite element models were generated using an existing computational framework. On average, the simulations correctly predicted 30.3% of the stem taper fretting wear area.

Imaging with DMM provided high-resolution pictures of the stem taper surfaces. However, these images do not readily distinguish between damaged and undamaged areas. Several scales have been developed for classifying damage on taper surfaces [12,28,30]. These scales facilitate standardized measures of taper fretting wear across the community. However, identifying regions of fretting wear or corrosion is often based on subjective measures and is dependent on the analyst. As such, there is the potential for bias and inconsistency. This study proposes an automated method for objectively identifying and quantifying damaged and undamaged taper surface areas. The DFT technique uses the periodic imaging process of the DMM to isolate damaged surfaces. The conical shape and reflective surface of the stem tapers produce photographs that are dark in the center and brighter toward the left and right edges (i.e., a circumferential brightness gradient). Stitching these photographs together produces axially oriented light-to-dark bands, with one band for each photograph in the circumferential direction. This local light-to-dark gradient was a useful artifact of photography. Although it prevented identification of damage by a set grayscale threshold value, the fretting wear disrupted the regular surface reflection and locally eliminated axial banding. Therefore, circumferentially plotting the grayscale intensity from DMM images revealed a consistent sinusoidal grayscale intensity in undamaged areas, and a disrupted (i.e., irregular) response in damaged areas. Consequently, DFTs were used to specify local frequency responses of the grayscale intensity, which were then processed to identify damaged regions. The DFT technique was able to identify fretting wear damage on all ten specimens. With further validation, this technique may provide a robust way of automating the recognition of fretting wear and corrosion on taper junctions.

Pixel-to-pixel comparisons were made between DFT and FWD damage maps. DFT areas ranged from 9.2 to 74.5 mm^2 with an average of 44.2 mm^2. FWD areas ranged from 34.1 to 51.5 mm^2 with an average of 43.5 mm^2. Qualitatively, FWD damage was generally concentrated near DFT damage such that FWD damage overlapped an average of 30.3% of the DFT damage. Magnitudes of the overlapping areas ranged from 0.0 to 32.3 mm^2 (corresponding percentages of 0.0 to 64.3%), indicating some models had much better predictive ability than others. This also shows that in some instances, the majority of the simulated FWD area does not overlap DFT identified damage. An average of 30.22 ($\pm$8.24) mm^2 of simulated FWD damage did not overlap with

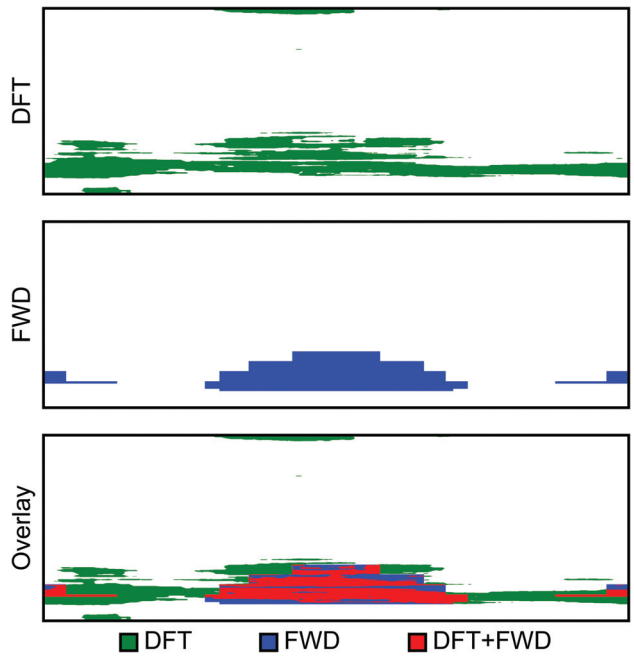

Fig. 7 DFT damage map generated from DMM images is compared to the FWD damage map determined using FEA. Both maps are discretized to have the same resolution so that the comparison can be made on a pixel-by-pixel basis. Areas of damage identified with the DFT technique are green. Areas of FWD damage determined from FEA are blue. The Overlay image indicates common area in red, where the FWD map overlaps the DFT map.

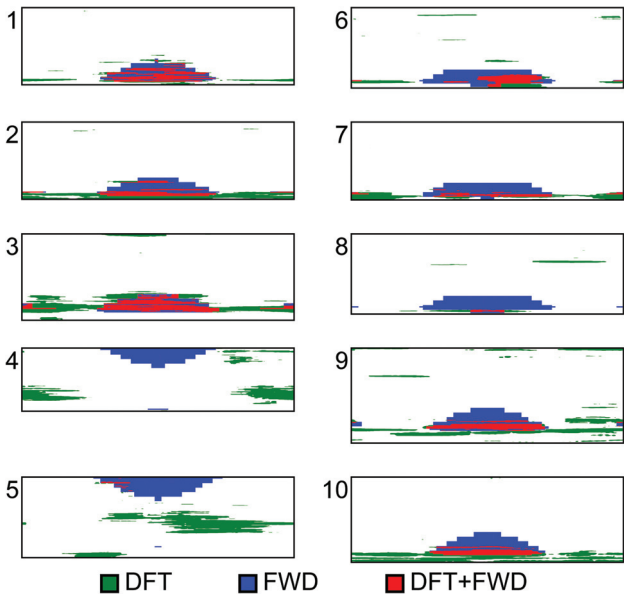

Fig. 8 Overlay images for all specimens. Areas of damage identified with the DFT technique are green. Areas of FWD damage determined from FEA are blue. Overlaying areas (common to DFT and FWD) are red.

observed DFT damage. This area represents incorrect damage predictions and highlights specificity as one of the biggest limitations of the model. Although areas of simulated FWD were often near DFT, the model's specificity can be improved.

Agreement between imaged fretting wear (DFT) and modeled FWD is influenced by the FWD threshold level. The continuous FWD maps were thresholded to produce a binary image in order to make a pixel-by-pixel comparison between imaged fretting wear and modeled FWD. The finite element models result in a continuous distribution of FWD over the taper surface. Selecting a threshold value is analogous to identifying the critical level of FWD, which correlates to physical fretting wear. The selected threshold was based on the amount of taper area identified as damaged with the DFT technique. The DFT technique calculated that an average of 7.7% of the taper surface areas experienced fretting wear. Using this average amount of experimental damage as a guide, FWD maps were thresholded at the upper 7.7%, with all FWD values greater than this threshold considered damaged, and all FWD values less than this threshold considered undamaged. The average FWD threshold level across all models was 32.98 J/m^2. The resulting amount of overlap between experiment (DFT) and finite element model (FWD) could then be interpreted as the level of model predictive ability. This method has limitations. Specimen fretting wear area ranged from 1.6 to 12.1%, so using the average 7.7% is an approximation. Increasing or decreasing the threshold value would increase or decrease the amount of FWD area, respectively. This could potentially make for increased or decreased overlap with DFT area. Implementing a threshold at a critical FWD value where fretting wear transitions from nonvisible to visible damage would be ideal. However, such a FWD value is not known. As such, the threshold value was rooted in an experimental observation, as opposed to an arbitrarily selected FWD magnitude. Future work could investigate the influence of threshold value on predictive ability as well as identification of a critical level of FWD at which fretting wear transitions from nonvisible to visible.

Contact location also influenced simulated FWD. The models predicted FWD distributions would shift from distal to proximal with respective shift in contact location of the stem-head constructs. Despite this consistent response, predictive ability was much higher for neutral and distally contacting specimens than proximally contacting. The reasons for this discrepancy are not clear, though it is likely attributable to the linear-elastic material model. It is possible that proximally contacting specimens are producing higher contact stresses due to the smaller contact area associated with the narrow proximal end of the taper. This could cause localized yielding, deformation, and fretting wear that the linear-elastic model is incapable of simulating. As such, proximally contacting specimens may be undergoing more complex fretting wear, leading to poor agreement between the proximally contacting finite element models and experimental constructs. Conversely, the greater contact area of the neutrally and distally contacting specimens may be undergoing primarily elastic deformation, leading to better agreement with the finite element model. Other simulations exhibited similar results to this study [41–44]. These models had pressure and wear maps with comparable distributions and concentrations to the present results. Like this investigation, others used linear-elastic material models. Some investigations also incorporated plasticity and/or simulated wear so surface degradation could be quantified through simulated fatigue loading. Also, like the present study, some simulations showed initial stress concentrations occurring on the distal-inferior surface of the taper. Wear was often concentrated on the inferior aspect of the taper and would move proximally and distally with respective changes in contact between stem and head. However, these models showed that stress and surface degradation could evolve over the time of cyclic fatigue loading, significantly affecting the location of fretting wear. Therefore, incorporating a more advanced material model (such as one with yielding and plasticity) may increase agreement with proximally contacting specimens. Overall, the proposed finite element model provides promising predictive ability for distally contacting tapers, and produces results that are consistent with similar FEA investigations.

This study has several limitations. The DFT technique developed here was effective in identifying damage on DMM images. However, this may be unique to the specimens and laboratory environment. Tapers had a reflective surface and a particular curvature such that high magnification images produced a banded effect when stitched together. Specimens made of other materials, having different surface finishes, or imaged under different lighting conditions, may not exhibit the vertical banding and thus not provide the periodic grayscale contrast needed for damage identification with DFTs. In its current form, the algorithm has only been qualified for identifying damage on reflective metallic tapers. Additional testing with different surface finishes and materials is needed to determine the robustness of the DFT technique. Additionally, the measurement system associated with DMM image acquisition is inconsistent. Image size measured via DMM ranged from 448.5 to 676.5 mm^2 despite nearly identical specimen geometry. Future work should focus on refining the imaging algorithm.

An increased sample size would have also been beneficial. In particular, an evenly distributed range of angular mismatches (proximal to distal) may provide greater insight to improve the predictive ability of the model, which would then increase our understanding of in vivo performance. Currently, the model shows the best predictions for neutral to distal contact, but it is not known at what angular mismatch this predictive ability breaks down. Additionally, a larger sample size would have allowed for separate groups of calibration and validation constructs. The current model has been calibrated ($E = 210$ GPa and $\nu = 0.3$) to the ten constructs to minimize extensometer displacement error. However, the calibrated model was not validated with a separate set of constructs. Therefore, the predictive ability of the model beyond the calibration constructs is unknown. Future efforts should include validating the predictive ability of the model on a separate sample of constructs.

The material model and specimen geometry are also limited. Materials were restricted to linear-elastic and isotropic behaviors. Fretting wear and damage are complex phenomena involving yielding, hardening, failure, material displacement/removal, and corrosion. Moreover, the finite element model assumes stem and head geometries are perfectly conical. Actual specimens will exhibit some out-of-roundness as well as irregular surface topography. The current model does not account for these factors. Future work could quantify geometric deviation and potentially correlate it to model predictive ability. Taken together, all these simplifications are likely contributing to the model's inability to accurately predict damage in proximally contacting tapers.

This study demonstrates that linear-elastic properties produce reasonable initial models to predict fretting in THA taper junctions. Moreover, a quantitative metric was developed for comparing experimental damage to modeled damage. This study serves as a base for subsequent levels of hierarchical validation. Future efforts should focus on progressive validation and improvement of the model framework, such as sequentially incorporating additional material model complexities like yielding, hardening, and surface evolution. Incrementally adding and validating individual model parameters will ensure the greatest level of confidence. Future models should also incorporate detailed surface topography of the experimental constructs. Surface profilometry has been used to characterize the roughness and deformation of the tapers. Measuring wear depth and volume could also serve to strengthen model validation. These data could be used to validate interfacial coefficients of friction or a finite element model incorporating plasticity or surface evolution.

Conclusion

Total hip arthroplasty constructs were cyclically loaded, thus inducing fretting wear at the taper junction between stem and

head. The stem taper surfaces were imaged using DMM and a novel DFT technique was developed to identify damaged surface area. Specimen-specific finite element models replicated the loading scenario and predicted FWD on the taper surfaces. The results demonstrate that:

(1) Identification of damage regions within a DMM image can be automated through a DFT approach.
(2) FWD as calculated by FEA can be used to approximate fretting wear in some metallic THA taper junctions, with the current model being a potential first step in subsequent hierarchical validation.
(3) Results were best for constructs exhibiting neutral to distal taper contact, with proximal contact and other factors requiring further investigation.

The DFT technique could be further developed by testing with additional materials, laboratory conditions, and nonlinear material behavior. With additional refinement, this approach may be useful to device manufacturers by complimenting current methods of estimating wear characteristics of THA constructs and to optimize designs for reduced wear.

Acknowledgment

The authors thank James C. Coburn for his contributions to the finite element model framework and its validation.

The authors also thank Exponent for performing the out of roundness measurements.

Funding Data

- FDA intramural funding supported the development of the finite element framework (Funder ID: 10.13039/100000038).
- FDA Center for Devices and Radiological Health Critical Path (FY2012CPOSEL22 and FY2013CPOSEL07; Funder ID: 10.13039/100000038).
- FDA Office of Women's Health (FY2014OWH5; Funder ID: 10.13039/100007238).

Nomenclature

DFT = discrete Fourier transform
DMM = digital mosaic method
f_D = dominant frequency
FEA = finite element analysis
FWD = Fretting work done
M = micromotion
P = contact pressure
THA = total hip arthroplasty

References

[1] Wolford, M. L., Palso, K., and Bercovitz, A., 2015, "Hospitalization for Total Hip Replacement Among Inpatients Aged 45 and Over: United States, 2000–2010," NCHS Data Brief, **186**, pp. 1–8.
[2] Steiner, C., Andrews, R., Barrett, M., and Weiss, A., 2012, "HCUP Projections: Mobility/Orthopedic Procedures 2003 to 2012," U.S. Agency for Healthcare Research and Quality, Rockville, MD, HCUP Projections, Report No. 2012-03.
[3] Barrack, R. L., 1994, "Modularity of Prosthetic Implants," J. Am. Acad. Orthop. Surg., **2**(1), pp. 16–25.
[4] Kop, A. M., Keogh, C., and Swarts, E., 2012, "Proximal Component Modularity in THA–At What Cost? An Implant Retrieval Study," Clin. Orthop. Relat. Res., **470**(7), pp. 1885–1894.
[5] Collier, J. P., Mayor, M. B., Williams, I. R., Surprenant, V. A., Surprenant, H. P., and Currier, B. H., 1995, "The Tradeoffs Associated With Modular Hip Prostheses," Clin. Orthop. Relat. Res., **311**, pp. 91–101.
[6] Hozack, W. J., Mesa, J. J., and Rothman, R. H., 1996, "Head-Neck Modularity for Total Hip Arthroplasty. Is It Necessary?," J Arthroplasty, **11**(4), pp. 397–399.
[7] Srinivasan, A., Jung, E., and Levine, B. R., 2012, "Modularity of the Femoral Component in Total Hip Arthroplasty," J. Am. Acad. Orthop. Surg., **20**(4), pp. 214–222.
[8] Higgs, G. B., Hanzlik, J. A., MacDonald, D. W., Gilbert, J. L., Rimnac, C. M., and Kurtz, S. M., and Implant Research Center Writing, C., 2013, "Is Increased Modularity Associated With Increased Fretting and Corrosion Damage in Metal-on-Metal Total Hip Arthroplasty Devices?: A Retrieval Study," J. Arthroplasty, **28**(Suppl. 8), pp. 2–6.
[9] Castro, F. P., Jr., Chimento, G., Munn, B. G., Levy, R. S., Timon, S., and Barrack, R. L., 1997, "An Analysis of Food and Drug Administration Medical Device Reports Relating to Total Joint Components," J. Arthroplasty, **12**(7), pp. 765–771.
[10] Collier, J. P., Mayor, M. B., Jensen, R. E., Surprenant, V. A., Surprenant, H. P., McNamar, J. L., and Belec, L., 1992, "Mechanisms of Failure of Modular Prostheses," Clin. Orthop. Relat. Res., **285**, pp. 129–139.
[11] Hernigou, P., Queinnec, S., and Flouzat Lachaniette, C. H., 2013, "One Hundred and Fifty Years of History of the Morse Taper: From Stephen A. Morse in 1864 to Complications Related to Modularity in Hip Arthroplasty," Int. Orthop., **37**(10), pp. 2081–2088.
[12] Goldberg, J. R., Gilbert, J. L., Jacobs, J. J., Bauer, T. W., Paprosky, W., and Leurgans, S., 2002, "A Multicenter Retrieval Study of the Taper Interfaces of Modular Hip Prostheses," Clin. Orthop. Relat. Res., **401**, pp. 149–161.
[13] Gilbert, J. L., Buckley, C. A., and Jacobs, J. J., 1993, "In Vivo Corrosion of Modular Hip Prosthesis Components in Mixed and Similar Metal Combinations. The Effect of Crevice, Stress, Motion, and Alloy Coupling," J. Biomed. Mater. Res., **27**(12), pp. 1533–1544.
[14] Hussenbocus, S., Kosuge, D., Solomon, L. B., Howie, D. W., and Oskouei, R. H., 2015, "Head-Neck Taper Corrosion in Hip Arthroplasty," Biomed. Res. Int., **2015**, pp. 1–9.
[15] Langton, D. J., Sidaginamale, R., Lord, J. K., Nargol, A. V., and Joyce, T. J., 2012, "Taper Junction Failure in Large-Diameter Metal-on-Metal Bearings," Bone Jt. Res., **1**(4), pp. 56–63.
[16] Cooper, H. J., Della Valle, C. J., Berger, R. A., Tetreault, M., Paprosky, W. G., Sporer, S. M., and Jacobs, J. J., 2012, "Corrosion at the Head-Neck Taper as a Cause for Adverse Local Tissue Reactions After Total Hip Arthroplasty," J. Bone Jt. Surg. Am., **94**(18), pp. 1655–1661.
[17] Carli, A., Politis, A., Zukor, D., Huk, O., and Antoniou, J., 2015, "Clinically Significant Corrosion at the Head-Neck Taper Interface in Total Hip Arthroplasty: A Systematic Review and Case Series," Hip Int., **25**(1), pp. 7–14.
[18] Whitehouse, M. R., Endo, M., Zachara, S., Nielsen, T. O., Greidanus, N. V., Masri, B. A., Garbuz, D. S., and Duncan, C. P., 2015, "Adverse Local Tissue Reactions in Metal-on-Polyethylene Total Hip Arthroplasty Due to Trunnion Corrosion: The Risk of Misdiagnosis," Bone Jt. J., **97-B**(8), pp. 1024–1030.
[19] Gilbert, J. L., Mehta, M., and Pinder, B., 2009, "Fretting Crevice Corrosion of Stainless Steel stem-CoCr Femoral Head Connections: Comparisons of Materials, Initial Moisture, and Offset Length," J. Biomed. Mater. Res. B Appl. Biomater., **88**(1), pp. 162–173.
[20] Kao, Y. Y., Koch, C. N., Wright, T. M., and Padgett, D. E., 2016, "Flexural Rigidity, Taper Angle, and Contact Length Affect Fretting of the Femoral Stem Trunnion in Total Hip Arthroplasty," J. Arthroplasty, **31**(9), pp. 254–258.
[21] Nassif, N. A., Nawabi, D. H., Stoner, K., Elpers, M., Wright, T., and Padgett, D. E., 2014, "Taper Design Affects Failure of Large-Head Metal-on-Metal Total Hip Replacements," Clin. Orthop. Relat. Res., **472**(2), pp. 564–571.
[22] Panagiotidou, A., Meswania, J., Hua, J., Muirhead-Allwood, S., Hart, A., and Blunn, G., 2013, "Enhanced Wear and Corrosion in Modular Tapers in Total Hip Replacement is Associated With the Contact Area and Surface Topography," J. Orthop. Res., **31**(12), pp. 2032–2039.
[23] Pennock, A. T., Schmidt, A. H., and Bourgeault, C. A., 2002, "Morse-Type Tapers: Factors That May Influence Taper Strength During Total Hip Arthroplasty," J. Arthroplasty, **17**(6), pp. 773–778.
[24] Rehmer, A., Bishop, N. E., and Morlock, M. M., 2012, "Influence of Assembly Procedure and Material Combination on the Strength of the Taper Connection at the Head-Neck Junction of Modular Hip Endoprostheses," Clin. Biomech. (Bristol, Avon), **27**(1), pp. 77–83.
[25] Heiney, J. P., Battula, S., Vrabec, G. A., Parikh, A., Blice, R., Schoenfeld, A. J., and Njus, G. O., 2009, "Impact Magnitudes Applied by Surgeons and Their Importance When Applying the Femoral Head Onto the Morse Taper for Total Hip Arthroplasty," Arch. Orthop. Trauma Surg., **129**(6), pp. 793–796.
[26] Duda, G. N., Elias, J. J., Valdevit, A., and Chao, E. Y., 1997, "Locking Strength of Morse Tapers Used for Modular Segmental Bone Defect Replacement Prostheses," Biomed. Mater. Eng., **7**(4), pp. 277–284.
[27] Schmidt, A. H., Loch, D. A., Bechtold, J. E., and Kyle, R. F., 1997, "Assessing Morse Taper Function: The Relationship Between Impaction Force, Disassembly Force, and Design Variables," Modularity of Orthopedic Implants, ASTM International, West Conshohocken, PA.
[28] Hothi, H. S., Matthies, A. K., Berber, R., Whittaker, R. K., Skinner, J. A., and Hart, A. J., 2014, "The Reliability of a Scoring System for Corrosion and Fretting, and Its Relationship to Material Loss of Tapered, Modular Junctions of Retrieved Hip Implants," J. Arthroplasty, **29**(6), pp. 1313–1317.
[29] Di Prima, M., Vesnovsky, O., Kovacs, P., Hopper, R., Ho, H., Engh, C., and Topoleski, L., 2015, "Comparison of Visual Assessment Techniques for Wear and Corrosion in Modular Hip Replacement Systems," Modularity and Tapers in Total Joint Replacement Devices, ASTM International, West Conshohocken, PA.
[30] Fricka, K. B., Ho, H., Peace, W. J., and Engh, C. A., Jr., 2012, "Metal-on-Metal Local Tissue Reaction is Associated With Corrosion of the Head Taper Junction," J. Arthroplasty, **27**(8), pp. 26–31.
[31] Shareef, N., and Levine, D., 1996, "Effect of Manufacturing Tolerances on the Micromotion at the Morse Taper Interface in Modular Hip Implants Using the Finite Element Technique," Biomaterials, **17**(6), pp. 623–630.
[32] Elkins, J. M., Callaghan, J. J., and Brown, T. D., 2014, "Stability and Trunnion Wear Potential in Large-Diameter Metal-on-Metal Total Hips: A Finite Element Analysis," Clin. Orthop. Relat. Res., **472**(2), pp. 529–542.

[33] Fallahnezhad, K., Farhoudi, H., Oskouei, R. H., and Taylor, M., 2016, "Influence of Geometry and Materials on the Axial and Torsional Strength of the Head-Neck Taper Junction in Modular Hip Replacements: A Finite Element Study," J. Mech. Behav. Biomed. Mater., **60**, pp. 118–126.
[34] Donaldson, F. E., Coburn, J. C., and Siegel, K. L., 2014, "Total Hip Arthroplasty Head-Neck Contact Mechanics: A Stochastic Investigation of Key Parameters," J. Biomech., **47**(7), pp. 1634–1641.
[35] ISO, 2010, *Implants for Surgery—Partial and Total Hip Joint Prostheses—Part 4: Determination of Endurance Properties and Performance of Stemmed Femoral Components*, International Organization for Standardization, Geneva, Switzerland, Standard No. ISO 7206–4.
[36] ASTM, 2014, *Standard Practice for Fretting Corrosion Testing of Modular Implant Interfaces: Hip Femoral Head-Bore and Cone Taper Interface*, American Society for Testing and Materials, West Conshohocken, PA, United States, Standard No. ASTM F1875–98.
[37] Niinomi, M., 2002, "Recent Metallic Materials for Biomedical Applications," Metall. Mater. Trans. A, **33**(3), pp. 477–486.
[38] Ratner, B. D., Hoffman, A. S., Schoen, F. J., and Lemons, J. E., "1.2 Bulk Properties of Materials," *Biomaterials Science—An Introduction to Materials in Medicine*, 2nd ed., Elsevier, San Diego, CA, p. 28.
[39] Hussein, M., Mohammed, A., and Al-Aqeeli, N., 2015, "Wear Characteristics of Metallic Biomaterials: A Review," Materials, **8**(5), pp. 2749–2768.
[40] Swaminathan, V., and Gilbert, J. L., 2012, "Fretting Corrosion of CoCrMo and Ti6Al4V Interfaces," Biomaterials, **33**(22), pp. 5487–5503.
[41] Bitter, T., Khan, I., Marriott, T., Lovelady, E., Verdonschot, N., and Janssen, D., 2018, "Finite Element Wear Prediction Using Adaptive Meshing at the Modular Taper Interface of Hip Implants," J. Mech. Behav. Biomed. Mater., **77**, pp. 616–623.
[42] Ashkanfar, A., Langton, D. J., and Joyce, T. J., 2017, "Does a Micro-Grooved Trunnion Stem Surface Finish Improve Fixation and Reduce Fretting Wear at the Taper Junction of Total Hip Replacements? A Finite Element Evaluation," J. Biomech., **63**, pp. 47–54.
[43] Ashkanfar, A., Langton, D. J., and Joyce, T. J., 2017, "A Large Taper Mismatch is One of the Key Factors Behind High Wear Rates and Failure at the Taper Junction of Total Hip Replacements: A Finite Element Wear Analysis," J. Mech. Behav. Biomed. Mater., **69**, pp. 257–266.
[44] English, R., Ashkanfar, A., and Rothwell, G., 2015, "A Computational Approach to Fretting Wear Prediction at the Head–Stem Taper Junction of Total Hip Replacements," Wear, **338–339**, pp. 210–220.